The Relationship of Local Environment, N-type, Spin State and Catalytic Functionality of Carbon-Hosted Fe$^{II/III}$-N$_4$ for the Conversion of CO$_2$ to CO

Yuxin Xie, Yuning Yang, Wanping Yang, Nian Liu, Xiaohua Chen[*]

Chongqing Key Laboratory of Theoretical and Computational Chemistry, School of Chemistry and Chemical Engineering, Chongqing University, Chongqing, 401331, P.R. China

Supporting Information

1. Corresponding energies details

To examine the thermodynamic stability of designed FeN$_4$C$_{56}$H$_{20}$, we computed the cohesive energy *(E$_{coh}$*, eV/atom) of all doped systems, following the definition:[s1]

$$E_{\text{coh}} = [xE_{Fe} + yE_N + zE_C + nE_H - E_{doped}]/(x + y + z + n)$$

where *E$_{Fe}$*, *E$_N$*, *E$_C$*, *E$_H$* and *E$_{doped}$* represent the total energies of isolated Fe, N, C, H and designed catalyst, respectively, while *x, y, z, n* denote the number of corresponding atoms.

The formation energies were calculated to evaluate the doping difficulty in energy for all relevant doped systems in this work, based on the definition:[s1]

$$E_\text{f} = E_\text{doped} - E_\text{defect-graphene} - \mu_\text{Fe} - x\mu_\text{N} - y\mu_\text{H}$$

where the *E$_\text{doped}$* and *E$_\text{defect-graphene}$* are the total energies of doped and carbon sheet without FeN$_4$H$_2$, respectively, μ_Fe, μ_N and μ_H are the chemical potentials of Fe, N and H, respectively. x and y are the number of corresponding atoms removed from the doped-carbon sheets. Specifically, chemical potentials of N and H are defined as total energy per atom in pristine free N$_2$ and H$_2$ molecule, respective. And the chemical potential of Fe denotes the energy of Fe atom in the respective ground-state bulk phase. All the parameters of the formation energies are obtained by carrying out Material Studio DMol^3 version 8.0.

The adsorption energy (*E$_{ad}$*) of the intermediates for CO$_2$RR is given by:[s1,s2,s3]

$$E_{ad} = E_{*+adsorbate} - E_* - E_{adsorbate}$$

Where *E$_{*+adsorbate}$*, *E$_*$* and *E$_{adsorbate}$* is the total electronic energy (non-ZPE corrected) of the adsorption system, the individual surface and adsorbate, respectively.

Material Studio DMol^3 version 8.0[s4,s5] was used here to perform all of the formation energy calculations. The generalized gradient approximation (GGA)[S6,S7] with Perdew-Burke-Ernzerhof (PBE) functional[s8] is employed as the exchange-correlation functional. We used a double-numeric

---

*The corresponding authors: Xiaohua Chen, chxh7@cqu.edu.cn

quality basis set with polarization functions (DNP). The size of the DNP basis set is comparable to Gaussian 6-31G**, but DNP is more accurate than a Gaussian basis set of the same size.[S9,S10] The convergence criteria included threshold values of 1×10^{-5} hartree, 0.002 hartree·Å^{-1}, and 0.005 Å for energy, force, and displacement convergence, respectively, while the self-consistent-field density convergence threshold value was defined as 1×10^{-5} hartree.

Gibbs free energy correction

The equilibrium potential is –0.11 and –0.20 V for the reduction reaction of $CO_2 \rightarrow CO$ and $CO_2 \rightarrow HCOOH$, respectively.[s11-s13] The two possible two-electron CO_2RR are:

$$CO_2 + 2(H^+ + e^-) \rightarrow CO + H_2O \tag{S1}$$

$$CO_2 + 2(H^+ + e^-) \rightarrow HCOOH \tag{S2}$$

The Gibbs free energies of total reactions are –0.22 and –0.40 eV for (S1) and (S2), respectively, based on the method used by Nørskov,[s14] which are used to correct the overall free energy changes for two different reactions. Specifically, the Gibbs free energy change (ΔG) is corrected as $\Delta G(CO) = G(CO) + G(H_2O) - G(CO_2) - 2G(H^+ + e^-) = -0.22$ eV for the CO formation and $\Delta G(HCOOH) = G(HCOOH) - G(CO_2) - 2G(H^+ + e^-) = -0.40$ eV for the HCOOH formation.

Reference
(s1) Chen, Z.; Liu, X.; Zhao, J.; Jiao, Y.; Yin, L., Strain effect on the catalytic activities of B-and B/N-doped black phosphorene for electrochemical conversion of CO to valuable chemicals. *Journal of Materials Chemistry A* 2020**, 8**, 11986-11995.
(s2) Deng, C.; He, R.; Wen, D.; Shen, W.; Li, M., Theoretical study on the origin of activity for the oxygen reduction reaction of metal-doped two-dimensional boron nitride materials. *PhysChemChemPhys* 2018**, 20**, 10240-10246;
(s3) Deng, C., He, R., Wen, D., Shen, W., Li, M, Theoretical Analysis of Oxygen Reduction Reaction Activity on Single Metal (Ni, Pd, Pt, Cu, Ag, Au) Atom Supported on Defective Two-dimensional Boron Nitride Materials. *Journal of Energy Chemistry* 2013**, 00**, 1-3.
(s4) Delley, B. *J. Chem. Phys.* 1990**, 92**, 508.
(s5) Delley, B. *J. Chem. Phys.* 2000**, 113**, 7756.
(s6) Orita, H.; Nakamura, I.; Fujitani, T. *Surf. Sci.* 2004, **571**, 102.
(s7) Orita, H.; Nakamura, I.; Fujitani, T. *J. Chem. Phys.* 2005, **122**, 014703.
(s8) Perdew, J. P.; Burke, K.; Ernzerhof, M. *Phys. Rev. Lett.* 1996, **77**, 3865.
(s9) Benedek, N. A.; Snook, I. K.; Latham, K.; Yarovsky, I. *J. Chem. Phys.* 2005, **122**, 144102.
(s10) Inada, Y.; Orita, H. *J. Comput. Chem.* 2008, **29**, 225.
(s11) Guo, L.; Guo, S. Mechanistic understanding of CO_2 reduction reaction towards C1 products by molecular transition metal porphyrin catalysts, Int. J. Hydrog. Energy, 2021, **46**, 10608−10623.
(s12) Tripkovic, V.; Vanin, M.; Karamad, M.; Björketun, M. E.; Jacobsen, K. W.; Thygesen, K. S.;

Rossmeisl, J. Electrochemical CO_2 and CO reduction on metal-functionalized porphyrin-like graphene, J. Phys. Chem. C, 2013, **117**, 9187−9195.

(s13) Varela, A. S.; Ju,W.; Bagger, A.; Franco, P.; Rossmeisl, J.; Strasser, P. Electrochemical reduction of CO_2 on metal-nitrogen-doped carbon catalysts, ACS Catal., 2019, **9**, 7270−7284.

(s14) Peterson, A. A.; Abild-Pedersen, F.; Studt, F.; Rossmeisl J.; Norskov, J. K. How copper catalyzes the electroreduction of carbon dioxide into hydrocarbon fuels. Energy Environ. Sci. 2010, **3**, 1311–1315.

2. Tables

Table S1. DFT calculated energy of each system relative to the energy of its corresponding spin ground state $(E_r)^a$ of the $Fe^{II}N_4C/Fe^{III}N_4C$ catalysts at different spin states (S: Singlet, T: Triplet, Q: Quintet, D: Doublet, Qu: Quartet, Se: Sextet). And the adsorption energy (E_{ad}) of CO_2 and CO molecule on the surface of the $Fe^{II}N_4C/Fe^{III}N_4C$ catalysts. All energy values are given in eV.

		$Fe^{II}N_4C_S$	$Fe^{II}N_4C_T$	$Fe^{II}N_4C_Q$	$Fe^{III}N_4C_D$	$Fe^{III}N_4C_{Qu}$	$Fe^{III}N_4C_{Se}$
armchair	E_r	2.24	0.00	0.51	0.00	0.02	0.89
	E_f	-12.89	-14.02	-13.42	-4.49	-3.88	-2.47
	E_{coh}	1.59	1.61	1.61	1.48	1.48	1.47
	$E_{ad}(*CO_2)$	-0.92	-0.21	-0.25	-0.35	-0.20	-0.53
	$E_{ad}(*CO)$	-1.48	-1.41	-0.37	-0.31	-0.22	-0.57
zigzag	E_r	1.83	0.00	0.40	0.00	0.06	0.73
	E_f	-15.35	-16.25	-15.57	-6.72	-6.14	-4.86
	E_{coh}	1.58	1.61	1.60	1.47	1.47	1.46
	$E_{ad}(*CO_2)$	-0.93	-0.46	-0.35	-1.39	-0.43	-0.34
	$E_{ad}(*CO)$	-1.58	-0.24	-0.26	-1.41	-0.45	-0.33
pyrrole	E_r	2.36	0.00	0.09	0.61	0.05	0.00
	E_f	-16.14	-17.39	-16.84	-6.88	-6.52	-5.56
	E_{coh}	1.47	1.50	1.50	1.32	1.33	1.33
	$E_{ad}(*CO_2)$	-1.09	-0.40	-0.51	-0.59	-0.58	-0.81
	$E_{ad}(*CO)$	-1.66	-1.03	-0.39	-0.92	-0.42	-0.37

[a] $E_r = E_{system} - E_{ground}$

Note: To further examine the relative thermodynamic stability and evaluate the doping difficulty for all systems, we calculated the cohesive energies and formation energies, which are all listed in Table S1. Note that the ground states of these catalysts have highest formation energies and maximum cohesive energies, suggesting that the $Fe-N_4$ motif of the ground state is more easily embedded in the carbon matrix. The structural differences between $Fe^{II/III}N_4C$-a (z) and $Fe^{II/III}N_4C$-p mainly originate from the structural stability determined by the formation and cohesive energies. The formation

energies of $Fe^{II/III}N_4C$-p are significantly larger than these of $Fe^{II/III}N_4C$-a and $Fe^{II/III}N_4C$-z, indicating that pyrrole-type Fe-N_4 moiety could be most easily embedded in the interior of carbon nanoribbon. In contrast, the cohesion energies of $Fe^{II/III}N_4C$-p are lower than $Fe^{II/III}N_4C$-a and $Fe^{II/III}N_4C$-z, revealed that $Fe^{II/III}N_4C$-p has a weaker structural stability due to the structural particularity of the pentatomic ring of pyrrole structure with excessive electron density forcing the Fe ion out-of-plane.

Table S2. DFT calculated energy of each system relative to its corresponding energy of spin ground state (E_r)[a] of the COOH absorbed on the surfaces of the $Fe^{II/III}N_4C$ catalysts in different spin states (S: Singlet, T: Triplet, Q: Quintet, D:Doublet, Qu: Quartet, Se: Sextet, Sep: Septet). All energy values are given in eV. Short transverse lines ($-$) indicate the intermediate could not stably adsorb at this site. All the energies are gained at the M06-2X/6-31G(d,p) calculation level.

	E_r (*COOH)				E_r (*COOH)		
	Fe site	N1 site	N2 site		Fe site	N1 site	N2 site
$Fe^{II}N_4C_D$-a	1.63	1.45	2.13	$Fe^{III}N_4C_S$-a	2.34	1.56	1.85
$Fe^{II}N_4C_{Qu}$-a	1.59	0.74	1.48	$Fe^{III}N_4C_T$-a	0.85	0.00	0.58
$Fe^{II}N_4C_{Se}$-a	1.80	0.00	2.51	$Fe^{III}N_4C_Q$-a	1.32	0.32	0.89
				$Fe^{III}N_4C_{Sep}$-a	1.69	0.38	0.00
$Fe^{II}N_4C_D$-z	1.48	0.00	1.65	$Fe^{III}N_4C_S$-z	3.34	1.51	3.75
$Fe^{II}N_4C_{Qu}$-z	1.67	0.04	0.98	$Fe^{III}N_4C_T$-z	1.56	0.00	2.35
$Fe^{II}N_4C_{Se}$-z	1.20	0.98	2.28	$Fe^{III}N_4C_Q$-z	2.69	0.48	1.76
				$Fe^{III}N_4C_{Sep}$-z	2.08	1.79	1.18
$Fe^{II}N_4C_D$-p	1.20	0.50	$-$	$Fe^{III}N_4C_S$-p	3.30	1.69	$-$
$Fe^{II}N_4C_{Qu}$-p	1.32	0.00	$-$	$Fe^{III}N_4C_T$-p	1.39	0.10	$-$
$Fe^{II}N_4C_{Se}$-p	1.34	0.10	$-$	$Fe^{III}N_4C_Q$-p	1.49	0.00	$-$
				$Fe^{III}N_4C_{Sep}$-p	1.28	0.26	$-$

Table S3. DFT calculated energy of each system relative to its corresponding energy of spin ground state (E_r)[a] of the HCOO absorbed on the surfaces of the $Fe^{II/III}N_4C$ catalysts in different spin states (S: Singlet, T: Triplet, Q: Quintet, D:Doublet, Qu: Quartet, Se: Sextet, Sep: Septet). All energy values are given in eV. Short transverse lines (—) indicate the intermediate could not stably adsorb at this site. All the energies are gained at the M06-2X/6-31G(d,p) calculation level.

	E_r (HCOO*)				E_r (HCOO*)		
	Fe site	N1 site	N2 site		Fe site	N1 site	N2 site
$Fe^{II}N_4C_D$-a	0.97	2.41	2.80	$Fe^{III}N_4C_S$-a	1.44	3.78	4.51
$Fe^{II}N_4C_{Qu}$-a	0.00	2.42	2.81	$Fe^{III}N_4C_T$-a	0.52	2.34	—
$Fe^{II}N_4C_{Se}$-a	0.05	1.63	—	$Fe^{III}N_4C_Q$-a	0.00	2.65	1.63
				$Fe^{III}N_4C_{Sep}$-a	0.54	1.76	2.00
$Fe^{II}N_4C_D$-z	1.06	1.54	—	$Fe^{III}N_4C_S$-z	1.54	3.16	—
$Fe^{II}N_4C_{Qu}$-z	0.12	1.56	—	$Fe^{III}N_4C_T$-z	0.00	1.40	2.12
$Fe^{II}N_4C_{Se}$-z	0.00	2.53	—	$Fe^{III}N_4C_Q$-z	1.13	1.91	2.09
				$Fe^{III}N_4C_{Sep}$-z	0.70	3.25	4.35
$Fe^{II}N_4C_D$-p	2.60	1.40	—	$Fe^{III}N_4C_S$-p	3.36	3.32	—
$Fe^{II}N_4C_{Qu}$-p	1.24	1.44	—	$Fe^{III}N_4C_T$-p	1.38	1.58	—
$Fe^{II}N_4C_{Se}$-p	0.00	1.54	—	$Fe^{III}N_4C_Q$-p	1.44	1.72	—
				$Fe^{III}N_4C_{Sep}$-p	0.00	2.43	—

Table S4. Relative energies (E_r, eV) of *H and the Gibbs free energy change of $* + H^+ + e^- \rightarrow$ *H (ΔG_{*H}, eV) on $Fe^{II}N_4C$-a, $Fe^{II}N_4C$-z, $Fe^{II}N_4C$-p in four different sites. All the energies are gained through the M06-2X/6-31G(d,p) calculation level.

		E_r		ΔG	
	Spin states	Fe-H	N-H	Fe-H	N-H
$Fe^{II}N_4C_L$-a	Doublet	1.65	0.77	-0.47	-1.34
$Fe^{II}N_4C_M$-a				0.65	-0.22
$Fe^{II}N_4C_M$-a	Quartet	1.87	0.79	0.61	-0.47
$Fe^{II}N_4C_H$-a				0.86	-0.22
$Fe^{II}N_4C_H$-a	Sextet	0.88	0	-0.05	-0.83
$Fe^{II}N_4C_L$-z	Doublet	2.24	0	1.57	-0.68
$Fe^{II}N_4C_M$-z				2.48	0.24
$Fe^{II}N_4C_M$-z	Quartet	0.80	0.03	1.62	0.85
$Fe^{II}N_4C_H$-z				1.82	1.05
$Fe^{II}N_4C_H$-z	Sextet	1.48	0.63	2.07	1.22
$Fe^{II}N_4C_L$-p	Doublet	1.95	0.04	-0.38	-2.28
$Fe^{II}N_4C_M$-p				0.78	-1.11
$Fe^{II}N_4C_M$-p	Quartet	2.07	0	1.64	-0.43
$Fe^{II}N_4C_H$-p				1.68	-0.38
$Fe^{II}N_4C_H$-p	Sextet	1.56	0.12	1.15	-0.29

Table S5. Relative energies (E_r, eV) of *H and the Gibbs free energy change of $* + H^+ + e^- \rightarrow$ *H (ΔG_{*H}, eV) on $Fe^{III}N_4C$-a, $Fe^{III}N_4C$-z, $Fe^{III}N_4C$-p in four different sites. All the energies are gained through the M06-2X/6-31G(d,p) calculation level.

		E_r		ΔG	
	Spin state	E_r	E_r	Fe-H	N-H
$Fe^{III}N_4C_L$-a	Singlet	2.68	1.75	2.17	1.24
$Fe^{III}N_4C_L$-a	Triplet	0.91	0	0.38	-0.52
$Fe^{III}N_4C_M$-a				1.69	0.47
$Fe^{III}N_4C_M$-a	Quintet	1.46	0.24	0.39	-0.51
$Fe^{III}N_4C_H$-a				2.12	0.90
$Fe^{III}N_4C_H$-a	Septet	1.28	1.69	1.51	1.10
$Fe^{III}N_4C_L$-z	Singlet	2.35	2.00	2.78	2.43
$Fe^{III}N_4C_L$-z	Triplet	1.08	1.42	1.48	1.81
$Fe^{III}N_4C_M$-z				2.08	0.76
$Fe^{III}N_4C_M$-z	Quintet	1.32	0	1.51	1.84
$Fe^{III}N_4C_H$-z				2.42	1.09
$Fe^{III}N_4C_H$-z	Septet	0.96	1.15	1.41	1.22
$Fe^{III}N_4C_L$-p	Singlet	4.96	2.46	3.56	1.06
$Fe^{III}N_4C_L$-p	Triplet	2.57	0	1.45	-1.12
$Fe^{III}N_4C_M$-p				1.40	-0.76
$Fe^{III}N_4C_M$-p	Quintet	2.27	0.10	1.17	-1.40
$Fe^{III}N_4C_H$-p				1.38	-0.79
$Fe^{III}N_4C_H$-p	Septet	2.33	0.25	1.88	-0.20

Table S6. The spin density on Fe for all the intermediates. Multiplicity is the whole system.

Intermediate	*	*COOH	*HCOO	$*CO-H_2O$	*COOH	*HCOO
Multiplicity	2	2	2	3	4	4
$Fe^{II}N_4C$-a	1.98	0.01	1.04	0.02	2.00	2.89
$Fe^{II}N_4C$-z	1.97	1.97	0.02	2.04	1.99	2.03
$Fe^{II}N_4C$-p	1.98	0.02	0.04	0.00	2.02	1.13

Intermediate	*	*COOH	*HCOO	$*CO-H_2O$
Multiplicity	5	6	5	5
$Fe^{II}N_4C$-a	3.09	3.83	2.93	2.04
$Fe^{II}N_4C$-z	1.99	2.00	2.94	2.09
$Fe^{II}N_4C$-p	1.98	2.02	2.80	1.11

Intermediate	*	*COOH	*HCOO	$*CO-H_2O$	*	*COOH
Multiplicity	2	3	3	2	4	5
$Fe^{III}N_4C$-a	1.97	2.02	1.97	0.02	2.00	2.00
$Fe^{III}N_4C$-z	1.97	1.98	2.96	0.00	1.98	2.03
$Fe^{III}N_4C$-p	0.00	2.01	1.17	-0.02	2.06	2.01

Intermediate	*HCOO	$*CO-H_2O$	*COOH	$*CO-H_2O$	*COOH	*HCOO
Multiplicity	5	4	6	6	7	7
$Fe^{III}N_4C$-a	2.88	0.03	3.11	2.04	3.86	2.88
$Fe^{III}N_4C$-z	2.07	2.05	3.12	2.22	2.04	2.88
$Fe^{III}N_4C$-p	1.16	3.05	1.98	3.15	3.11	3.86

Note: The spin state of Fe is not consist with the multiplicity of the whole system. This may be attributed to the two possible factors. One is that the FeN_4C materials have good π-conjugate structures, which cause spin density delocalizes over the sheet. The other is that the unavoidable spin contamination for open-shell systems causes by the DFT calculations.

3. Figures
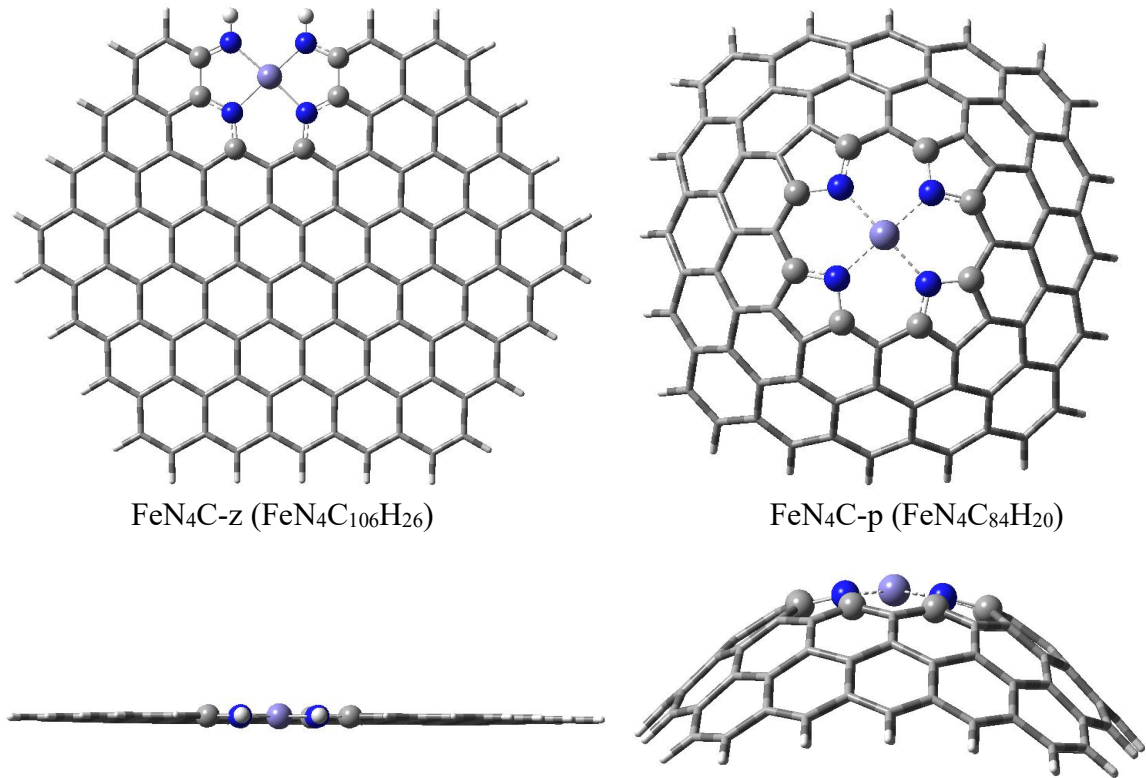
Figure S1. Top and side views of big FeN$_4$C models: pyridine-type zigzag-edge FeN$_4$C-z (137 atoms) and pyrrole-type bulk FeN$_4$C-p (109 atoms). Color code: C, gray; N, blue; Fe, purple; O, red; H, white.

Comparing with the small size of the FeN$_4$C-z mode, the big size of FeN$_4$C-z (FeN$_4$C$_{106}$H$_{26}$) still keep the square-planar geometry structure. However, the big FeN$_4$C-p (FeN$_4$C$_{84}$H$_{20}$) mode also breaks the planer structure after the optimized calculations with the Fe$^{2+/3+}$ ion protruding from the plane
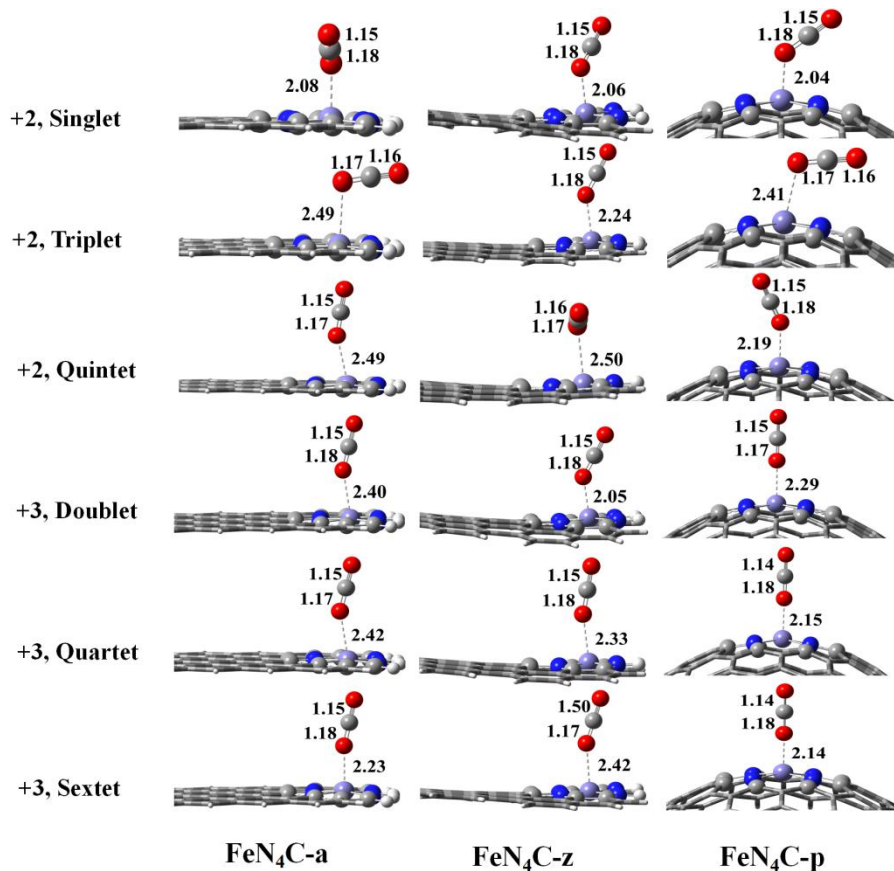
Figure S2. Adsorbed CO_2 configurations on singlet ($Fe^{II}N_4C_S$), triplet ($Fe^{II}N_4C_T$) and quintet ($Fe^{II}N_4C_Q$) spin state of $Fe^{II}N_4C$-a (z, p) catalyst and on doublet ($Fe^{III}N_4C_D$), quartet ($Fe^{III}N_4C_{Qu}$) and sextet ($Fe^{III}N_4C_{Se}$) spin state of $Fe^{III}N_4C$-a (z, p) catalyst. The bond lengths are given in Å.
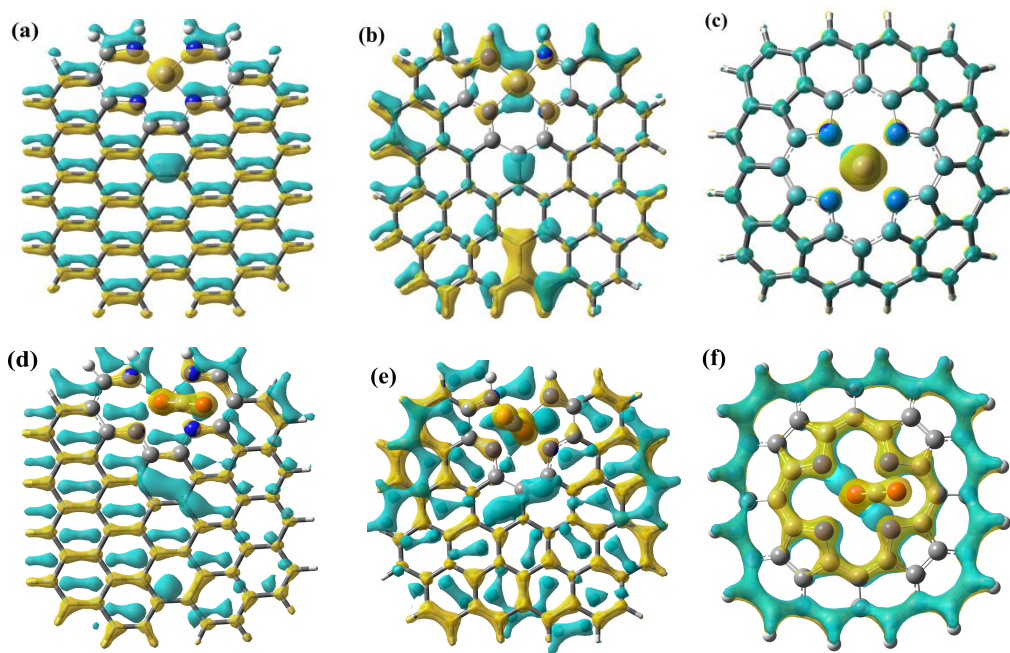
Figure S3. Electron density difference ($\Delta\rho$) for (a) FeN$_4$C-a, (b)FeN$_4$C-z, (c) FeN$_4$C-p and (d) FeN$_4$C-a-CO$_2$, (e) FeN$_4$C-z-CO$_2$, (f) FeN$_4$C-p-CO$_2$ with low spin state under +2 oxidation state, where $\Delta\rho = \rho_{(slab+ads)} - \rho_{(slab)} - \rho_{(ads)}$. Yellow and cyan bubbles represent electron accumulation and depletion. Electron density difference analyses reveal that weak electron transfer takes place from the surrounding C-atoms to Fe for the FeN$_4$ embedded graphite (Figure S2 a-c) and partial electron transfer occurs from the FeN$_4$C sheet to the CO$_2$ moiety for the CO$_2$ binding FeN$_4$C systems (Figure S2 d-e), which is beneficial for the activation of CO$_2$.
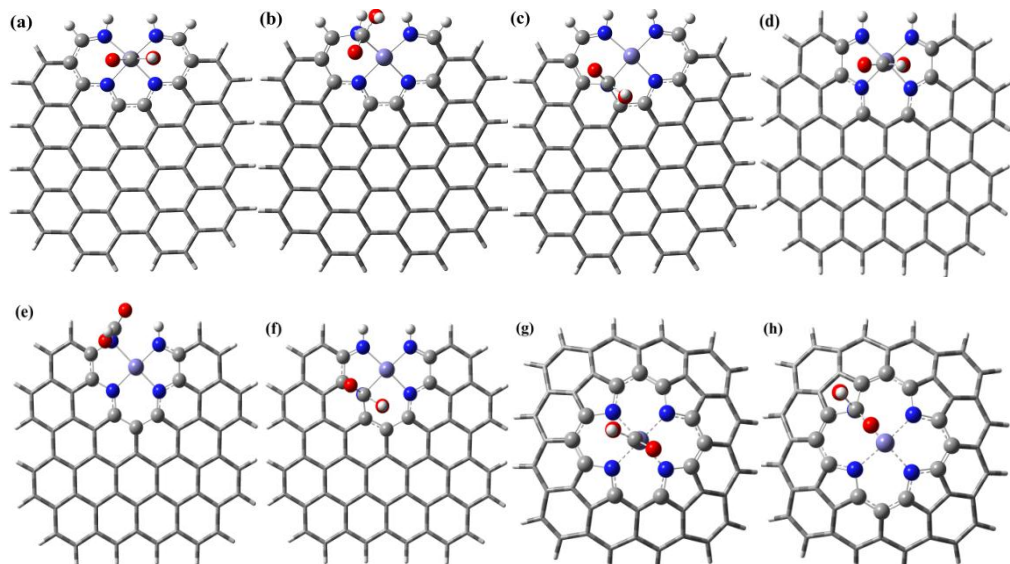
Figure S4. Adsorption configurations of the *COOH on (a-c) FeN$_4$C-a, (d-f) FeN$_4$C-z and (g-h) FeN$_4$C-p with different adsorption sites. Corresponding adsorption energies are summarized in the Table S2-S3.
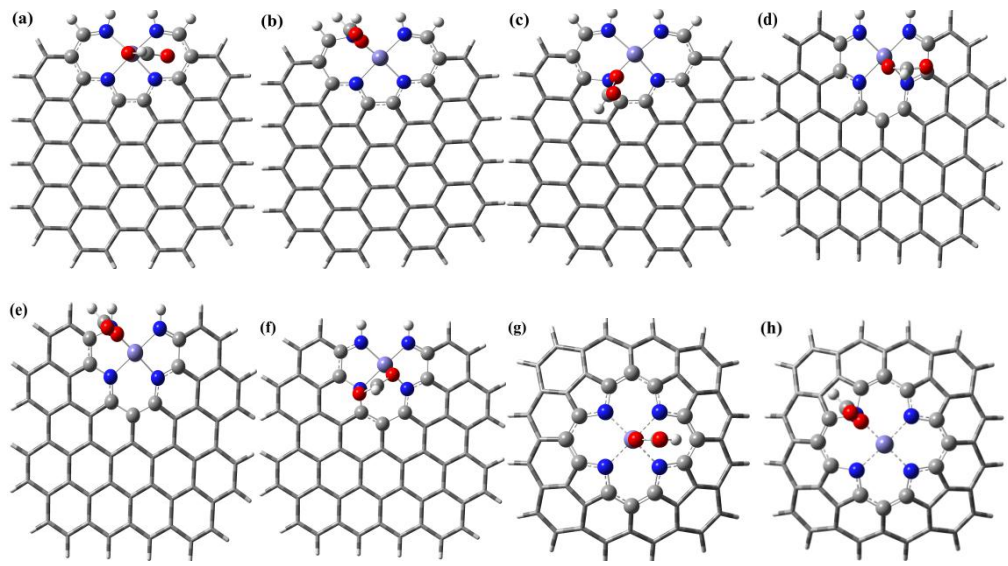
Figure S5. Adsorption configurations of the HCOO* on (a-c) FeN$_4$C-a, (d-f) FeN$_4$C-z and (g-h) FeN$_4$C-p with different adsorption sites. Corresponding adsorption energies are summarized in the Table S2-S3.
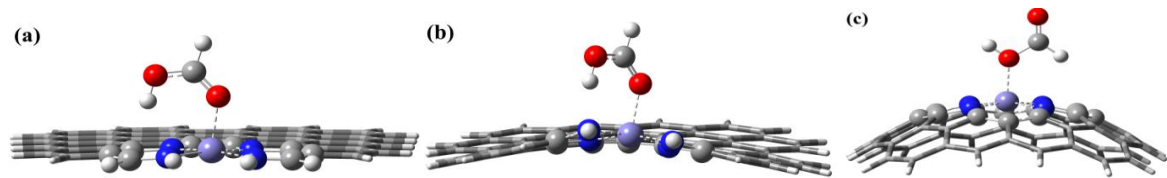
Figure S6. Adsorption configurations of the *HCOOH on (a) FeN$_4$C-a, (b) FeN$_4$C-z and (c) FeN$_4$C-p with different adsorption sites. Here, the structures of HCOOH adsorption on N1/N2 atoms are not stable. Corresponding adsorption energies are summarized in the Table S2.
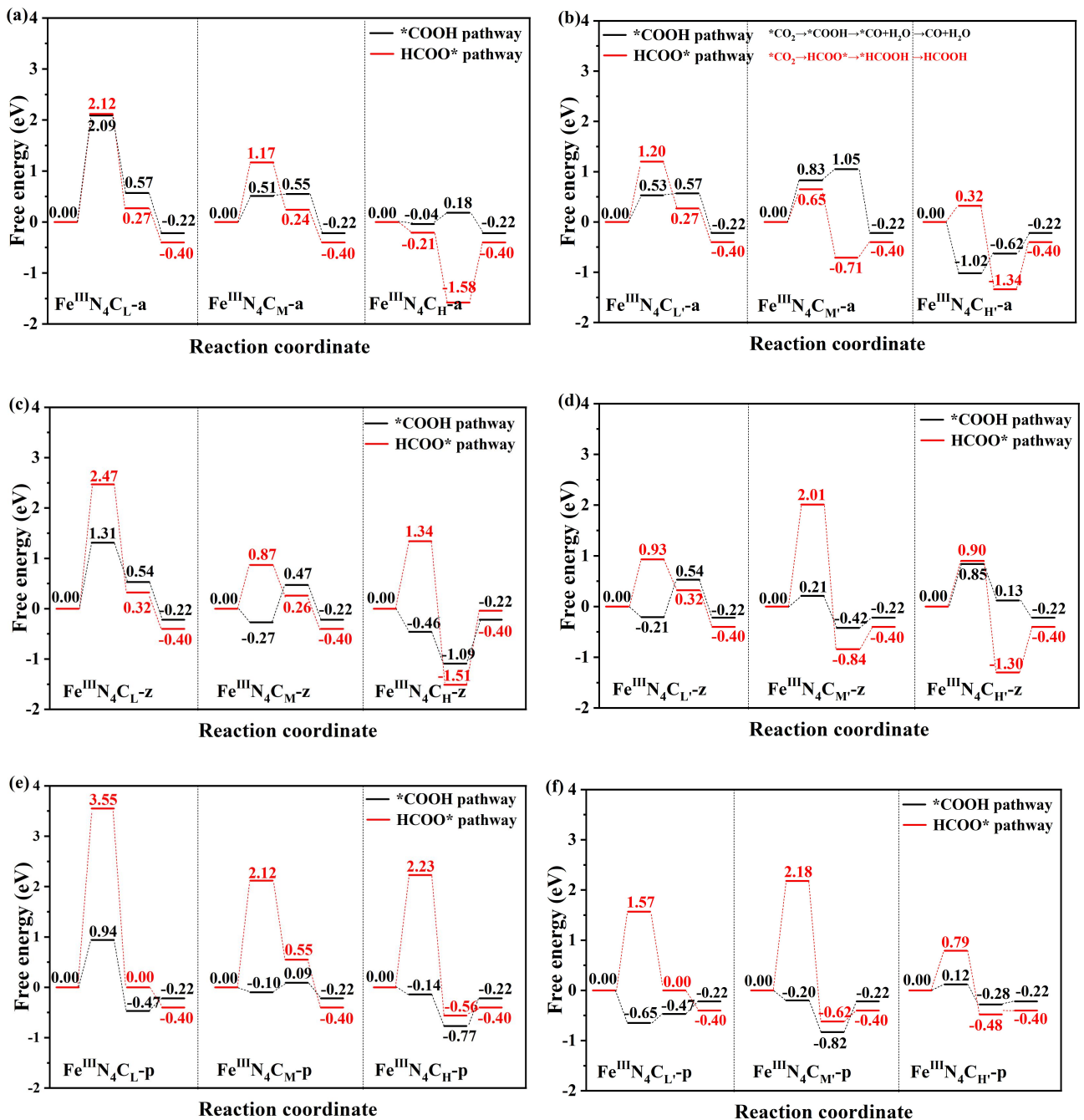
Figure S7. Gibbs free energy diagrams for CO₂RR toward CO and HCOOH products on spin-coupling (a) Fe^{III}N$_4$C-a, (c) Fe^{III}N$_4$C-z, (e) Fe^{III}N$_4$C-p and spin-uncoupling (b) Fe^{III}N$_4$C-a, (d) Fe^{III}N$_4$C-z, (f) Fe^{III}N$_4$C-p at 0 V vs RHE. The black and red line represent the CO₂ conversion through *COOH pathway and HCOO* pathway, respectively. The numbers on horizontal lines denote the energetic position of key intermediates. The changing multiplicities of Fe^{III}N$_4$C system in spin-coupling manner are 2-1-2 for the low spin, 4-3-2 for the medium spin, 6-5-4 for the high spin and the corresponding changing multiplicities in spin-uncoupling manner are 2-3-2 for the low spin, 4-5-4 for the medium spin, 6-7-6 for the high spin when the *CO₂ sequentially obtains two H atoms.
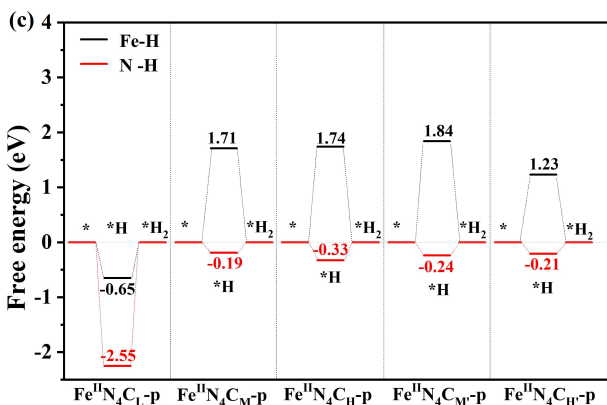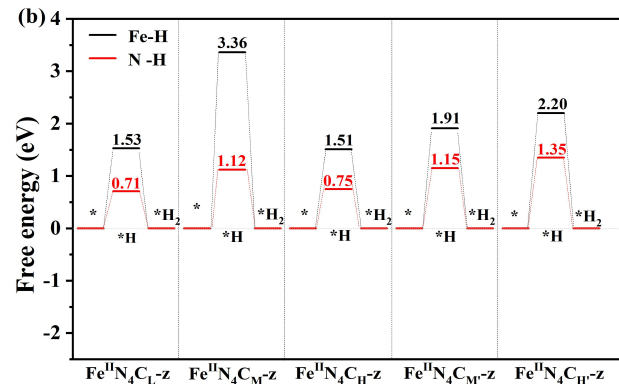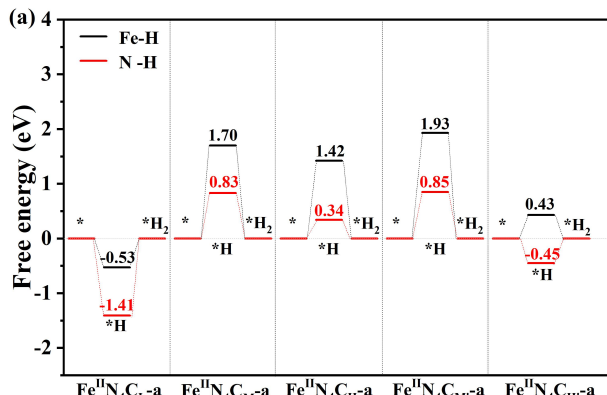
Figure S8. Gibbs free energy diagrams of the simulated HER at 0 V (vs. RHE): (a) $Fe^{II}N_4C$-a at the different spin states, (b) $Fe^{II}N_4C$-z at the different spin states, (c) $Fe^{II}N_4C$-p at the different spin states. The negative free energy values of *H on the N-site support the formation of the N-H bonds on the surfaces of $Fe^{II}N_4C$-a and $Fe^{II}N_4C$-p, which can serve as proton donors for the electrochemical reduction of CO_2.
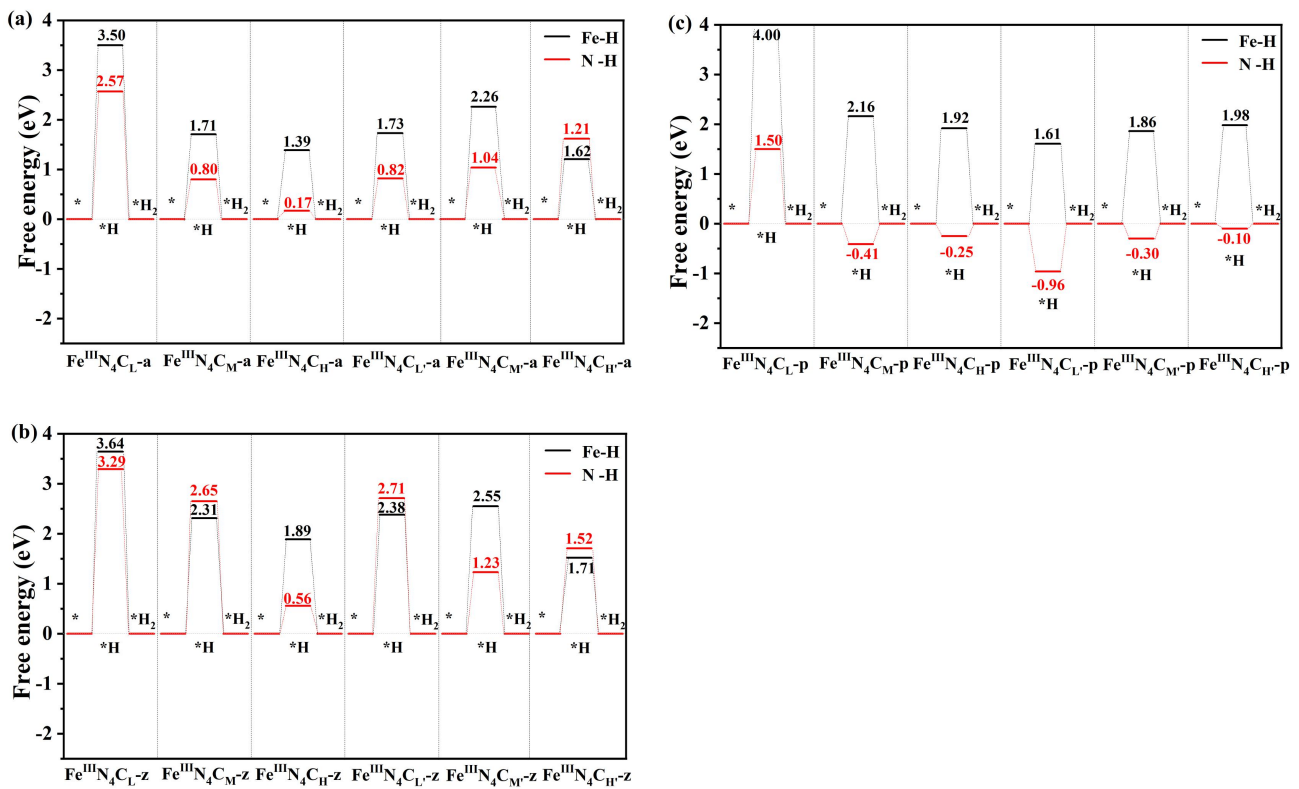
Figure S9. Gibbs free energy diagrams of the simulated HER at 0 V (vs. RHE): (a) $Fe^{III}N_4C$-a at the different spin states, (b) $Fe^{III}N_4C$-z at the different spin states and (c) $Fe^{v}N_4C$-p at the different spin states.
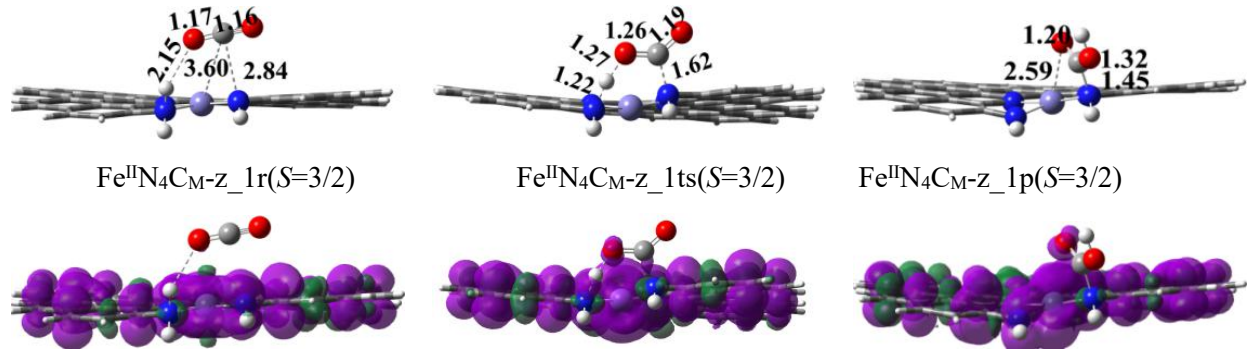
Figure S10. Structures for the reactant ($Fe^{II}N_4C_M$-z_1r), the transition state ($Fe^{II}N_4C_M$-z_1ts) and the product ($Fe^{II}N_4C_M$-z_1p) of the COOH formation with the corresponding distribution of spin density. All the structures are gained through the M06-2X/6-31G(d,p) optimizations. The bond lengths are given in Å. The isosurface value of spin densities is 0.001 au.
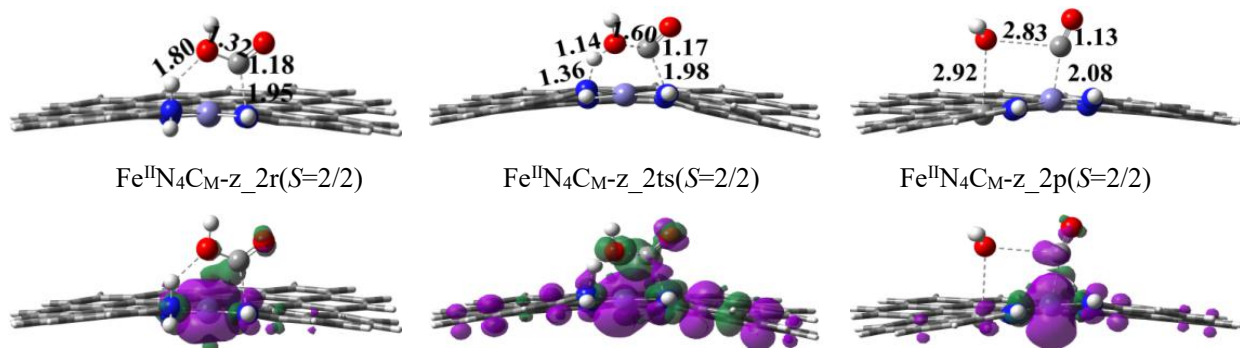
Figure S11. Structures for the reactant ($Fe^{II}N_4C_M$-z_2r), the transition state ($Fe^{II}N_4C_M$-z_2ts) and the product ($Fe^{II}N_4C_M$-z_2p) of the CO formation with the corresponding distribution of spin density. All the structures are gained through the M06-2X/6-31G(d,p) optimizations. The bond lengths are given in Å. The isosurface value of spin densities is 0.001 au.
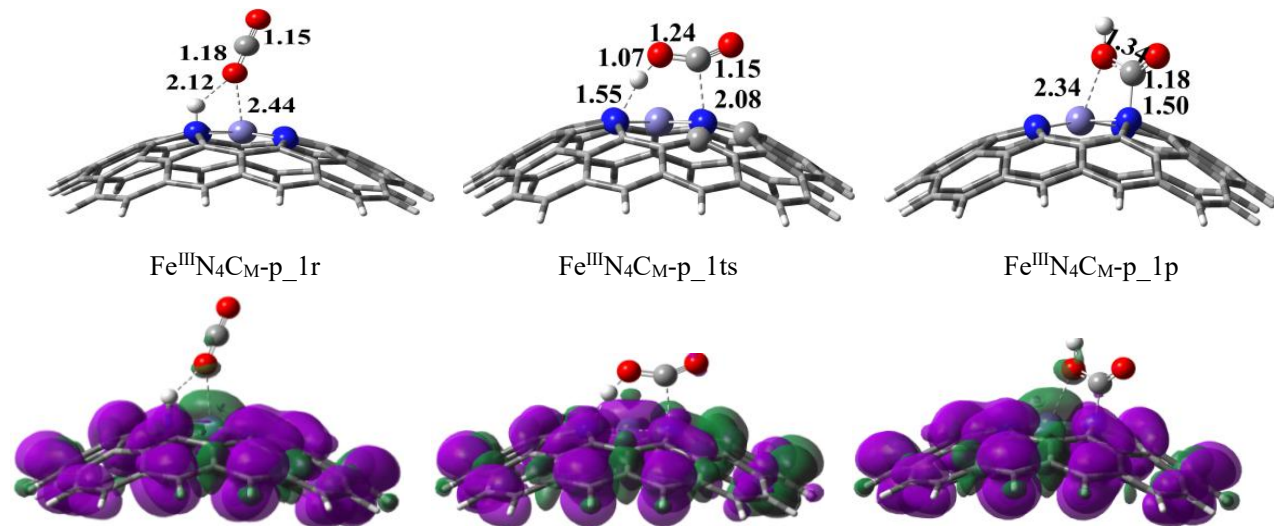
Figure S12. Structures for the reactant ($Fe^{III}N_4C_M$-p_1r), the transition state ($Fe^{III}N_4C_M$-p_1ts) and the product ($Fe^{III}N_4C_M$-p_1p) of the COOH formation with the corresponding distribution of spin density. All the structures are gained through the M06-2X/6-31G(d,p) optimizations. The bond lengths are given in Å. The isosurface value of spin densities is 0.001 au.

$Fe^{III}N_4C_M$-p_2r(S=1/2) $Fe^{III}N_4C_M$-p_2tsa(S=1/2) $Fe^{III}N_4C_M$-p_2p(S=1/2)
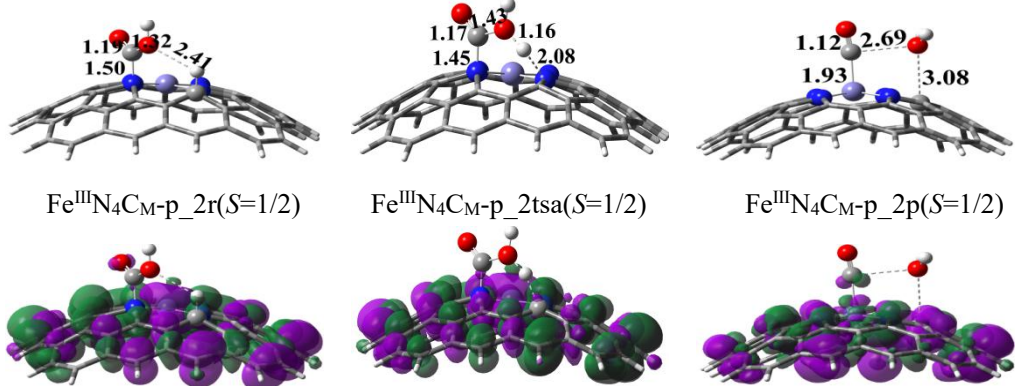
Figure S13. Structures for the reactant ($Fe^{III}N_4C_M$-p_2r), the transition state ($Fe^{III}N_4C_M$-p_2ts) and the product ($Fe^{III}N_4C_M$-p_2p) of the CO formation with the corresponding distribution of spin density. All the structures are gained through the M06-2X/6-31G(d,p) optimizations. The bond lengths are given in Å. The isosurface value of spin densities is 0.001 au.

When the COOH moiety is further reduced to CO and H_2O, our DFT calculations revealed that the N−H can not serve as the proton donor for the pyrrole-type $Fe^{III}N_4C_M$-p. Therefore, we considered the ambient C−H to act as a proton donor since the C atoms around the Fe-N$_4$ moiety can stably absorb hydrogen atoms.
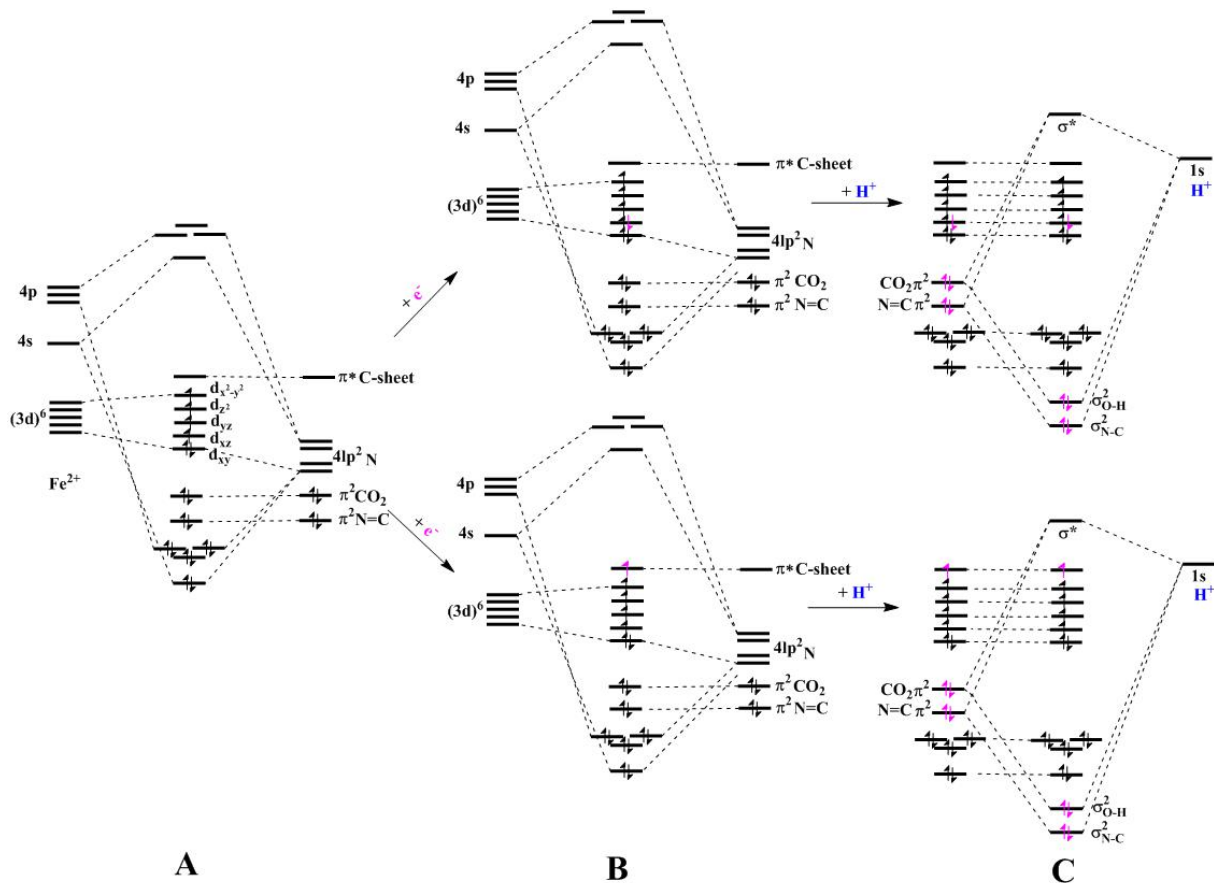
Scheme S1. Diagrams of molecular orbital energy levels for the formation of $Fe^{II}N_4C_H$-a (**A**), the possible molecular orbital for $Fe^{II}N_4C_H$-a gaining an electron (**B**) and the protonation of the CO_2 O_1-site (**C**). The coplanar FeN_4 and C-sheet causes the energy of π^* of C-sheet to be nearly equal to the d-orbitals of Fe^{2+}, which may accept an electron, as shown in **B**. The protonation of a O-atom of CO_2 accompanies ET from the electrode sheet to CO_2, which is achieved by breaking a π bond of CO_2 to form the new O-H σ bond and breaking planar N=C π bond to produce a new N-C σ bond, as shown in **C**.